Hubbard parameters for programmable tweezer arrays

Hao-Tian Wei [1,2,*] Eduardo Ibarra-García-Padilla [1,2,3,4] Michael L. Wall [5] and Kaden R. A. Hazzard [1,2,3]

[1]*Department of Physics and Astronomy, Rice University, Houston, Texas 77005-1892, USA*
[2]*Rice Center for Quantum Materials, Rice University, Houston, Texas 77005-1892, USA*
[3]*Department of Physics, University of California, Davis, California 95616, USA*
[4]*Department of Physics and Astronomy, San José State University, San José, California 95192, USA*
[5]*The Johns Hopkins University Applied Physics Laboratory, Laurel, Maryland 20723, USA*

The experimental realization of Fermi-Hubbard tweezer arrays opens a new stage for engineering fermionic matter, where programmable lattice geometries and Hubbard model parameters are combined with single-site imaging. In order to use these versatile experimental Fermi-Hubbard models as quantum simulators, it is crucial to know the Hubbard parameters describing them. Here we develop methods to calculate the Hubbard model parameters of arbitrary two-dimensional lattice geometries: The tunneling t, on-site potential V, and interaction U for multiple bands and for both fermions and bosons. We show several examples. One notable finding is that a finite array of equally strong and separated individual tweezer potentials actually sums to give a nonperiodic total potential and thus spatially nonuniform Hubbard parameters. We demonstrate procedures to find trap configurations that equalize these parameters. More generally, these procedures solve the inverse problem of calculating Hubbard parameters: Given desired Hubbard parameters, find trap configurations to realize them. These methods will be critical tools for using tunnel-coupled tweezer arrays.

I. INTRODUCTION

The Fermi-Hubbard model has been widely studied over a half century as it captures a key feature of strongly correlated matter, the competition between kinetic and interaction energy in a lattice, which is relevant to almost all quantum materials. Although it is the simplest model for studying interacting fermions on a lattice, it displays rich physics, such as a metal-insulator crossover, antiferromagnetic order, strange metallicity, and potential d-wave superconductivity [1–6]. Due to its richness, the Fermi-Hubbard model is of fundamental interest and is studied in numerous quantum simulation platforms.

Ultracold atoms in optical lattices have been paradigmatic quantum simulators of Hubbard models. Numerous long-studied Fermi-Hubbard phenomena have been observed and explored using optical lattice experiments [7–11]. Recently, quantum gas microscopes capable of resolving single lattice sites have further extended the capability of quantum control and quantum simulation [12–14].

Nevertheless, optical lattice Hubbard models have important limitations, most apparently that they are restricted to periodic potentials since they are formed by interfering lasers. Additionally, optical lattice experiments have yet to reach temperatures deep into the regime characteristic of antiferromagnetism or potential superconducting order [15,16].

Recently, atoms in tunnel-coupled optical tweezer arrays have provided a platform for simulating Hubbard models

with programmable one-dimensional (1D) [17–22] and two-dimensional (2D) [23] geometries and dramatically new capabilities for reaching lower temperatures and entropies. In particular, using near-unit filling and postselection techniques to prepare low-entropy initial states for adiabatic preparation may allow experiments to access previously inaccessible low-temperature phases [21,23].

However, to utilize tunnel-coupled tweezers as quantum simulators, one needs to know the programed Hubbard model parameters: On-site potentials, tunneling rates, and interactions. Theory is necessary, as measuring or calibrating all of these parameters experimentally is challenging—cross effects between traps make independently measuring parameters difficult.

Although, in principle, these parameters can be determined from the single-particle eigenstates, the calculations are significantly more complicated than for optical lattices. In both cases, one first determines the single-particle eigenstates and then uses these to calculate localized Wannier functions from which Hubbard parameters are obtained. For tweezers, however, there are obstacles in both steps. This has restricted calculations to simple analytic treatments [24]; although useful, this gives only rough order-of-magnitude estimates, and it also misses qualitative features, such as the correct scaling of the tunneling with respect to trap depth.

The first obstacle is the challenge of finding the eigenstates. Tweezer arrays are nonseparable, in contrast to many optical lattices, which reduce to one-dimensional problems. Additionally, tweezers have no spatial periodicity, increasing the size of systems that must be considered. Despite these challenges, discrete-variable-representation (DVR) methods

*htwei@rice.edu

[25–30] that were first applied to two tunnel-coupled tweezers in Ref. [31] are able to efficiently find the eigenstates. DVR methods combine the exponential convergence of spectral methods with the sparsity of real-space finite-difference methods.

The second obstacle is that determining appropriately localized Wannier functions is more involved than for lattices, even after the single-particle eigenbasis is found. For optical lattices, the Wannier functions are simply Fourier transforms of the eigenstates because of the periodicity of the lattice. While, for only two identical tweezers, one can determine the Wannier functions from reflection symmetry [31], for general tweezer arrays finding the unitary basis transform that gives localized Wannier functions is more involved.

In this paper, we develop a method to compute the Hubbard parameters for tunnel-coupled tweezer arrays given the trap parameters. We illustrate this method on several 1D and 2D geometries and for multiband models. The method works by combining the DVR method for single-particle eigenstates with Riemannian manifold optimization techniques to compute maximally localized Wannier functions that have been developed in condensed-matter and quantum chemistry [32]. In the context of ultracold matter, similar methods were used to construct Wannier functions for 1D double-well and 2D honeycomb lattices [33,34], but for these periodic lattices Bloch eigenstates can be obtained by diagonalizing a single unit cell, so DVR techniques are less necessary, and Wannier functions are translations of each other. Research on nonperiodic quasicrystalline optical lattices exists as well [35]. However, this work does not apply the more efficient DVR method, and the way it constructs Wannier functions may lose the maximal locality. Other research, in which an efficient and precise method of tuning tight-binding parameters in 1D optical lattices was developed, encounters difficulties in obtaining the Hubbard interaction parameter and faces challenges when attempting to apply to higher dimensions [36].

One important finding of our example calculations is that even when tweezers are nominally uniform—the Gaussian beams have equal spacings, waists, and strengths—the resulting Hubbard parameters vary spatially because the total trapping potential differs site to site due to the finite size of the array. This presents an obstacle to simulating translationally invariant many-body systems, which have uniform Hubbard parameters. We therefore propose and demonstrate techniques to equalize the Hubbard parameters.

This paper is organized as follows. Section II presents the method and demonstrates Hubbard parameter calculations in optical tweezer arrays. We then describe our methods and propose two experimental protocols to increase control of Hubbard parameters in Sec. III and demonstrate these suffice to achieve spatially uniform Hubbard parameters. Section IV gives the conclusions.

II. HUBBARD PARAMETER CALCULATIONS

This section shows the methods and results of our Hubbard parameter calculations. Section II A presents the theoretical description of tunnel-coupled tweezer arrays and outlines our approach to calculating Hubbard parameters. Section II B describes the DVR method to obtain single-particle eigenstates.
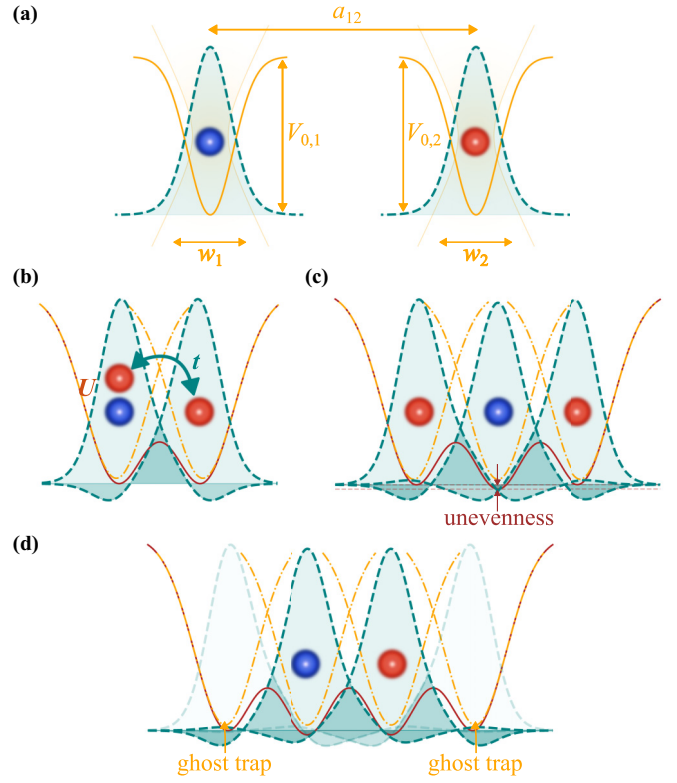

FIG. 1. Hubbard model realized in an optical tweezer array. (a) Tweezers are brought together in an array, with tunable trap depths $V_{0,i}$, spacings a_{ij}, and waists w_i, where indices index tweezers. Throughout, we treat the waists w_i as fixed unless otherwise noted since they are not tunable in current experiments [21,23]. Only in Sec. III D do we present a speculative proposal for trap engineering, in which we allow the waists to be tunable. (b) Under suitable conditions, the array is described by a low-energy effective Hubbard model with tunnelings t_{ij} and interactions U_i. (c) Due to cross talk, setting distances between traps and trap depths equal gives potentials, interactions, and tunneling rates that are inhomogeneous: The existence of the right trap changes the energy barrier between the left and center traps, for example. (d) Two methods to equalize Hubbard parameters are to adjust trap waists (in addition to locations and depths), as shown in (a), and to add "ghost traps" as in (d).

Section II C describes how to construct the maximally localized Wannier functions (MLWFs) from which the Hubbard parameters are calculated. Section II D then calculates and discusses the Hubbard parameters in various 1D and 2D lattice geometries. This exhibits the power of the tweezer platform and the efficiency and flexibility of our algorithm.

A. Tweezer arrays and outline for obtaining Hubbard parameters

The optical tweezer array is made of tightly focused Gaussian lasers, each of which induces an attractive potential [Fig. 1(a)],

$$V_{\text{trap}}(\boldsymbol{r}) = \frac{-V_0}{1 + \frac{z^2}{z_R^2}} \exp\left[\sum_{\xi=x,y} \frac{-2\xi^2}{\left(1 + \frac{z^2}{z_{R,\xi}^2}\right) w_\xi^2}\right], \quad (1)$$

where $\mathbf{r} = (x, y, z)$ is the Cartesian coordinate vector, ξ goes over only x and y transversal coordinates, V_0 is the trap depth, and w_x (w_y) and $z_{R,x}$ ($z_{R,y}$) are the trap waist and Rayleigh range in the x (y) direction. z_R is the "effective" Rayleigh range, defined by $\frac{1}{z_R^2} = \frac{1}{2}(\frac{1}{z_{R,x}^2} + \frac{1}{z_{R,y}^2})$. The trapping laser beams' locations and depths are programmable via deflections from a driven acousto-optic modulator (AOM) or potentially phase masking by a spatial-light modulator (SLM).

Bringing traps close enough together results in coherent tunnel coupling and in the right regime (described in what follows) gives a system described by a Fermi-Hubbard model [Fig. 1(b)]. The continuum Hamiltonian of atoms in the tweezer array is

$$H = H_0 + H_{\text{int}}$$

$$= \int d^d\mathbf{r}\, \psi^\dagger(\mathbf{r})\left[-\frac{\hbar^2}{2m}\nabla^2 + V_{\text{total}}(\mathbf{r})\right]\psi(\mathbf{r})$$

$$+ \frac{1}{2}\int d^d\mathbf{r}\, d^d\mathbf{r}'\, \psi^\dagger(\mathbf{r})\psi^\dagger(\mathbf{r}')V_{\text{int}}(\mathbf{r} - \mathbf{r}')\psi(\mathbf{r}')\psi(\mathbf{r}), \quad (2)$$

with total trapping potential

$$V_{\text{total}}(\mathbf{r}) = \sum_i V_{\text{trap},i}(\mathbf{r} - \mathbf{R}_i), \quad (3)$$

where $\mathbf{R}_i$ are the beam centers, $\hbar$ is the reduced Planck's constant, m is the atom mass, $\psi(\mathbf{r})$ [$\psi^\dagger(\mathbf{r})$] is the annihilation (creation) operator, and $V_{\text{int}}(\mathbf{r} - \mathbf{r}')$ is the interaction, which in atomic systems, where the typical particle separation is large compared to the interaction range, is

$$V_{\text{int}}(\mathbf{r} - \mathbf{r}') = \frac{4\pi\hbar^2 a_s}{m}\delta(\mathbf{r} - \mathbf{r}'), \quad (4)$$

where a_s is the s-wave scattering length. In principle, this interaction needs to be regularized, but for what we will do this unregularized form suffices since we will only use matrix elements in a finite basis of analytic functions. Longer-range interactions, like those that occur in ultracold molecules [37–39] and Rydberg-dressed atoms [40–42], can be incorporated into our theory straightforwardly.

Under suitable conditions, the continuum Hamiltonian, Eq. (2), is equivalent to a Hubbard Hamiltonian. Specifically, when the interaction strength and temperature are weak compared to energy gaps to excited states out of the manifold that we will keep to describe the Hubbard limit (analogous to "band gaps" in infinite periodic systems) and the number of particles is sufficiently low that single-particle states above this gap are not occupied, we can project Eq. (2) to the states necessary for an accurate description of the physics, which is often only a few bands or even a single band. Then Eq. (2) is

$$H_{\text{FH}} = -\sum_\mu \sum_{ij} t_{ij\mu} a_{i\mu}^\dagger a_{j\mu} + \sum_\mu \sum_i V_{i\mu} n_{i\mu}$$

$$+ \sum_{\mu\nu\delta\sigma} \sum_{ijkl} U_{ijkl;\mu\nu\delta\sigma} a_{i\mu}^\dagger a_{j\nu}^\dagger a_{k\delta} a_{l\sigma}, \quad (5)$$

where μ, ν, δ, and σ index the "bands"; i, j, k, and l index lattice sites; $a_{i\mu}$ ($a_{i\mu}^\dagger$) is the operator that annihilates (creates) an atom on an orbital $W_{i\mu}(\mathbf{r})$, which is related to the field
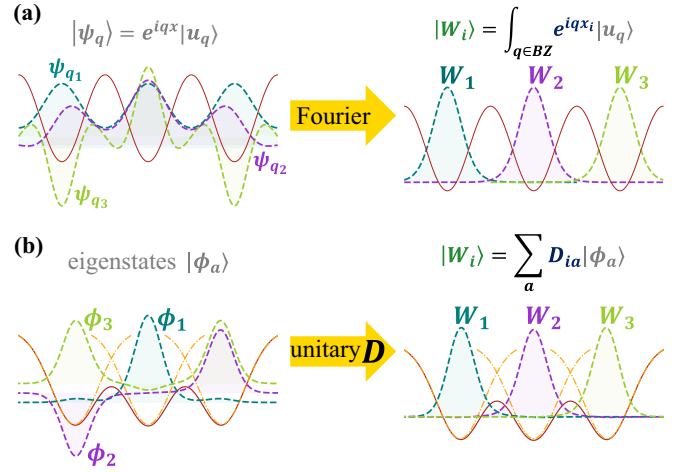

FIG. 2. Maximally localized Wannier functions. (a) In a typical optical lattice the Wannier functions are Fourier transforms of the Bloch wave functions of the bands of interest (usually lowest energy), while (b) in tweezer arrays, the Wannier functions are unitary transforms D of the relevant single-particle eigenstates (usually lowest energy), where D is chosen to produce the maximally localized set of Wannier functions, as measured by the cost function (12). Maximal localization ensures that the tunneling and interactions in the effective Hubbard model resulting from this basis can be truncated to short distances.

operators via the transformation

$$\psi(\mathbf{r}) = \sum_{i\mu} W_{i\mu}(\mathbf{r})a_{i\mu}; \quad (6)$$

and the Hubbard parameters are given by

$$t_{ij\mu} = -\int d^d\mathbf{r}\, W_{i\mu}^*(\mathbf{r})\left[-\frac{\hbar^2}{2m}\nabla^2 + V_{\text{total}}(\mathbf{r})\right]W_{j\mu}(\mathbf{r}), \quad (7)$$

$$V_{i\mu} = \int d^d\mathbf{r}\, W_{i\mu}^*(\mathbf{r})\left[-\frac{\hbar^2}{2m}\nabla^2 + V_{\text{total}}(\mathbf{r})\right]W_{i\mu}(\mathbf{r}), \quad (8)$$

$$U_{ijkl;\mu\nu\delta\sigma} = \frac{4\pi\hbar^2 a_s}{m}\int d^d\mathbf{r}\, W_{i\mu}^*(\mathbf{r})W_{j\nu}^*(\mathbf{r})W_{k\delta}(\mathbf{r})W_{l\sigma}(\mathbf{r}). \quad (9)$$

In general, the set of orbitals $\{W_{i\mu}(\mathbf{r})\}$ can be an arbitrary single-particle basis spanning the truncated space. However, it is useful to choose $W_{i\mu}(\mathbf{r})$ to be as localized as possible (by some measure introduced later), referred to as maximally localized Wannier functions, in which case $t_{ij\mu}$ and $U_{ijkl;\mu\nu\delta\sigma}$ can be truncated by discarding matrix elements between sites far enough apart in real space. In sufficiently deep lattices, it is an excellent approximation to truncate $t_{ij\mu}$ to nearest neighbors and $U_{ijkl;\mu\nu\delta\sigma}$ to on-site interactions, in which case we will denote it $U_{i;\mu\nu\delta\sigma}$. We will often suppress the spatial indices if the parameters are uniform and suppress the band index in the single-band case.

In infinite periodic lattices, the MLWFs are simply Fourier transforms of the single-particle eigenstates (Bloch wave functions), as shown in Fig. 2(a). The situation for optical tweezer arrays is more complicated, and more general unitary transformations from the single-particle eigenstates are required, as illustrated in Fig. 2(b)].

Our method, detailed in the next two sections, is therefore to (1) solve for the single-particle eigenstates, (2) find the MLWFs by finding the unitary transforms that give MLWFs in the eigenstate basis truncated to the desired low-energy bands, and (3) compute the Hubbard parameters with Eqs. (7), (8), and (9).

B. Discrete-variable representations

We employ the DVR method, following Ref. [31], to calculate the single-particle eigenstates with the lowest energies. The DVR method solves the Schrödinger equation in a basis of position basis states at grid points $\boldsymbol{r}_n$ (inside some spatial region) projected onto a low-momentum subspace. It maintains the exponential convergence of spectral methods and sparsity of methods that use finite-difference derivatives on real-space finite grids. All matrix elements are simple to obtain analytically. The sparse Hamiltonian can be diagonalized by the Lanczos algorithm to obtain the lowest-energy eigenstates. Besides the benefits above, symmetries, such as spatial reflection and rotation, can be easily incorporated into the choice of DVR basis to reduce the size of the matrix. The DVR method was shown to be an effective method for treating atoms in optical tweezers [23,31].

We choose the DVR basis in a box on a Cartesian grid of points. The method has two convergence parameters (for each Cartesian direction) associated with the basis choice: The size of the box and the grid spacing. We use a DVR grid-point spacing $(0.15, 0.15, 0.36)w_x$ and set the distance from the outermost trap centers to the system boundaries to $L_0 = (3, 3, 7.2)w_x$. An assessment of the convergence is given in Appendix A. We find that the Hubbard parameters presented in this paper are likely converged to a relative accuracy of 10^{-8} or better.

In our calculations, we make use of spatial-reflection symmetries in the x, y, and z directions. The lattice is on the $z = 0$ plane, so it is z reflection symmetric, and the coordinate origin is set such that the lattices presented in this paper have x- and y-direction reflection symmetries. Unless otherwise mentioned, we calculate the z-reflection-even sector only to find the lowest-energy states. For 1D lattices, the lattices sites are on the $y = z = 0$ line, so we further only consider the y- and z-reflection-even sectors.

C. Maximally localized Wannier functions

Given the eigenstates of the DVR calculation obtained using the methods in the last section, we now describe how to obtain the MLWF, essentially following the techniques in Ref. [32]. We truncate the eigenstates to those in the "bands" of interest. For a single-band model, it suffices to truncate to a number of eigenstates equal to the number of traps. In the present paper, we truncate by keeping the lowest-energy states, but other truncation schemes could be used.

In this truncated eigenbasis $\{|\phi_a\rangle\}_\mu$ chosen for the μth band, we seek a new maximally localized basis,

$$|W_{i\mu}\rangle = \sum_{a \in A_\mu} D_{ia}^{(\mu)} |\phi_a\rangle, \tag{10}$$

where i indexes sites, $D_{ia}^{(\mu)}$ is a unitary matrix within the μth band, and A_μ is the low-energy subset of the eigenbasis picked to form the μth band. $D_{ia}^{(\mu)}$ is chosen to minimize the sum of spatial spreads of the Wannier functions,

$$\Omega_\mu = \sum_i \left[\langle W_{i\mu}| r^2 |W_{i\mu}\rangle - \sum_\xi \langle W_{i\mu}| r_\xi |W_{i\mu}\rangle^2 \right], \tag{11}$$

where $r_\xi = x, y, z$. Other similar cost functions can be used, as described in Ref. [32], but all should give equivalent results when the Hubbard-regime approximations described above are valid. For numerical purposes, it is convenient to work with an equivalent form obtained by subtracting the unitarily invariant part $\sum_\xi \text{tr}_i[P_\mu r_\xi (1 - P_\mu) r_\xi]$, where the trace tr_i is over all $W_{i\mu}$ for the given μ and $P_\mu = \sum_i |W_{i\mu}\rangle \langle W_{i\mu}|$ is the projector onto the μth band,

$$\tilde{\Omega}_\mu = \sum_{i \neq j} \sum_\xi | \langle W_{i\mu}| r_\xi |W_{j\mu}\rangle |^2$$
$$= \text{tr}_i[X'^2 + Y'^2 + Z'^2], \tag{12}$$

where pure off-diagonal matrices X', Y', and Z' are defined as, for example, $X'_{ii} = 0$ and $X'_{i \neq j} = \langle W_{i\mu}| x |W_{j\mu}\rangle$. It is worth noting that the cost function is always non-negative, and zero value is taken if all the matrices X', Y', and Z' are diagonalized simultaneously. For one dimension, since only X' is nonzero, we make use of this fact and perform eigendecomposition to derive $D_{ia}^{(\mu)}$ for better performance. In higher dimensions, these matrices do not, in general, commute in the DVR basis since it is an incomplete basis, and therefore, numerical minimization is needed. But as shown in Appendix B, it can be proven that $\tilde{\Omega}_\mu$ does not depend on the phase of the matrix elements of $D_{ia}^{(\mu)}$, so the latter can be reduced to an orthogonal matrix. The minimization over orthogonal $D_{ia}^{(\mu)}$ for each μ can be done by established Riemannian manifold optimization algorithms, implemented by the PYMANOPT package [43].

After constructing the MLWF by obtaining $D_{ia}^{(\mu)}$ for every band, we can now directly calculate Hubbard parameters t and V from (7) and (8). These equations give

$$V_{i\mu} = \sum_a \epsilon_a |D_{ia}^{(\mu)}|^2, \tag{13}$$

$$t_{ij\mu} = - \sum_a \epsilon_a (D_{ia}^{(\mu)})^* D_{ja}^{(\mu)} \quad i \neq j, \tag{14}$$

and

$$U_{i;\mu\nu\delta\sigma} = \frac{4\pi \hbar^2 a_s}{m} \sum_{abcd} (D_{ia}^{(\mu)} D_{ib}^{(\nu)})^* D_{ic}^{(\delta)} D_{id}^{(\sigma)}$$
$$\times \int d^d \boldsymbol{r} \, \phi_a^*(\boldsymbol{r}) \phi_b^*(\boldsymbol{r}) \phi_c(\boldsymbol{r}) \phi_d(\boldsymbol{r}), \tag{15}$$

where ϵ_a is the energy of the single-particle eigenstate $|\phi_a\rangle$ and the integral is done numerically.

Since $\sum_{i\mu} V_{i\mu}$ is irrelevant in a particle-number-conserving system, in practice we shift $V_{i\mu}$ to the average value over all V_{i1} in the lowest $\mu = 1$ band.

D. Results

This section presents the results of calculating Hubbard parameters in various 1D and 2D lattices. For concreteness, the trap parameters are those from recent experiments with ^{6}Li atoms [21,23], but all of our methods are general. For rectangular lattices, the lattice constant is set to $a_x = 1550\,\text{nm}$ along the x direction and $a_y = 1600\,\text{nm}$ in the y direction [44]. For triangular-type lattices, e.g., kagome and honeycomb with defects, we use $a = 1550\,\text{nm}$ for all neighbor bonds. We use a $\lambda = 780\,\text{nm}$ laser wavelength and use an isotropic trap waist $w = w_x = w_y = 1000\,\text{nm}$ to generate circular traps with depth $V_0 = h \times 52.26\,\text{kHz}$ (h is Planck's constant). This results in an isotropic Rayleigh range in the z direction of $z_R = \frac{\pi w^2}{\lambda} = 4028\,\text{nm}$. The s-wave scattering length is $a_s = 93.66\,\text{nm}$. These are the parameters used in our calculations throughout the paper unless mentioned otherwise.

Figure 3 shows the Hubbard parameters calculated for five example geometries in the single-band limit. Figures 3(a) and 3(b) show chains and rectangular lattices, small versions of geometries routinely realized in optical lattices. Figures 3(c) and 3(d) show geometries that are more challenging, but possible, to realize in an optical lattice: A 2×2 Lieb lattice [45] and a kagome lattice [46,47]. Finally, Fig. 3(e) shows a geometry that is straightforward to create in tweezers that would be extraordinarily difficult or impossible to realize in an optical lattice, a honeycomb lattice with a Stone-Wales defect [48]. For all the calculations the manifold optimizations [and matrix diagonalization for Fig. 3(a)] converge to machine precision for the resulting MLWFs. These calculations all run in no more than around 1 min on a laptop. The majority of the time is spent on diagonalizing the DVR matrices.

In addition to demonstrating the efficacy of the DVR + MLWF method described in Secs. II A–II C, these results allow us to assess the accuracy of range truncating the tunneling and interactions in Eq. (5). Figure 3(a) shows that the tunneling amplitudes decay rapidly with increasing distance for the 1D chain. The same is true for U_{ijkl}, where we find the on-site U_i are two orders of magnitude larger than any U involving two or more sites. These justify the effective Hubbard model description.

Higher bands can be included in the Hubbard models if desired, and the methods employed here work without modification. Figure 4 illustrates this for two-band Hubbard parameters for a 3×3 rectangular lattice consisting of two lowest-energy bands: The first is spanned by MLWFs that are approximately single-trap ground states, and the second is spanned by the first excited state, which is odd under z reflections. Given the reflection symmetries of two bands, the only nonzero interband $U_{\mu\nu\delta\sigma}$ are $U_{\mu\nu\nu\mu}$ and $U_{\mu\mu\nu\nu}$ with $\mu \neq \nu$, and they are equal because all MLWFs are real. This result shows the power of the DVR + MLWF calculation method. Access to higher bands could pave the way to simulating multiorbital models, an important aspect of real materials.

An interesting feature revealed by Fig. 3 is that Hubbard parameters vary spatially over the tweezer arrays, despite these tweezers' equal spacing and depth, due to the cross talk illustrated in Fig. 1(c). This shows the need to adjust trap parameters to achieve uniform t, U, and V, a task we take up in Sec. III. We note, however, that the nonuniformity is largely concentrated near the edge of the system, as shown in Figs. 3(a) and 3(b), inspiring one of our protocols to equalize Hubbard parameters discussed in detail in Sec. III.

III. EQUALIZING HUBBARD PARAMETERS

For quantum simulations, often, we are interested in translation-invariant models, but Sec. II showed that equally spaced and equal-depth traps do not lead to spatially uniform Hubbard parameters. This is natural because optical tweezer arrays, in contrast to optical lattices, lack translation invariance. The cross talk between traps breaks the trap uniformity, as shown in Fig. 1(c). This effect is particularly severe at the boundaries. So whether and how trap parameters can be chosen to equalize the Hubbard parameters are important questions.

A. Method

One approach to equalizing the trap parameters is to introduce a cost function measuring how unequal the parameters are and to use optimization algorithms to minimize this over the space of trap parameters: The trap center positions $\boldsymbol{r}_i$ and the individual trap depths V_{0i}. We use the cost function

$$C = \frac{1}{\tilde{t}^2} \sum_q \frac{1}{N_q} \sum_i (q_i - \tilde{q})^2, \tag{16}$$

where $q = t_x, t_y, V$, and U labels the Hubbard parameters being equalized, $\{\tilde{q}\}$ are target values for the parameters (we allow separate tunnelings t_x and t_y for anisotropic lattices), i indexes sites for U and V and indexes bonds for t_x and t_y, N_q labels the number of Hubbard parameters of kind q, and $\tilde{t}$ is the smaller of $\tilde{t}_x$ and $\tilde{t}_y$. This characterizes the parameter fluctuations compared to the most sensitive energy scale in the model. The optimization algorithms we use are the sequential least-squares programming (SLSQP) method in the SCIPY package and principal axis (PRAXIS) method in the NLOPT package in the PYTHON programming language. We apply both methods and choose the better minimum.

This cost function depends on the target Hubbard parameters $\{\tilde{q}\}$. One cannot simply choose these arbitrarily, as there are constraints, for example, on how large parameters such as the tunnelings can be. For example, for two traps, there is a maximum "tunneling" when the two traps are focused at the same location. In practice, in order to stay in the Hubbard regime, the tunneling needs to be set much lower than this maximum. Additionally, choosing target values for which a known trap configuration gives Hubbard parameters reasonably close to the target values will make the optimization more efficient, reducing the number of Hubbard parameter calculations required and reducing the chances of getting stuck in a local, rather than global, minimum.

To obtain the target $\{\tilde{q}\}$, we have found the following procedure works well. We first calculate Hubbard parameters for initial trap configurations in the geometry desired, and then we choose the largest interaction in the lattice as our target $\tilde{U}$ and the smallest tunneling in the x and y directions as our target $\tilde{t}_x$ and $\tilde{t}_y$. To achieve the desired U/t_a values we can scale the geometry. The target value for V is set to zero (recall that as mentioned in Sec. II C, the zero of V is shifted in every calculation to the average of the lowest band).
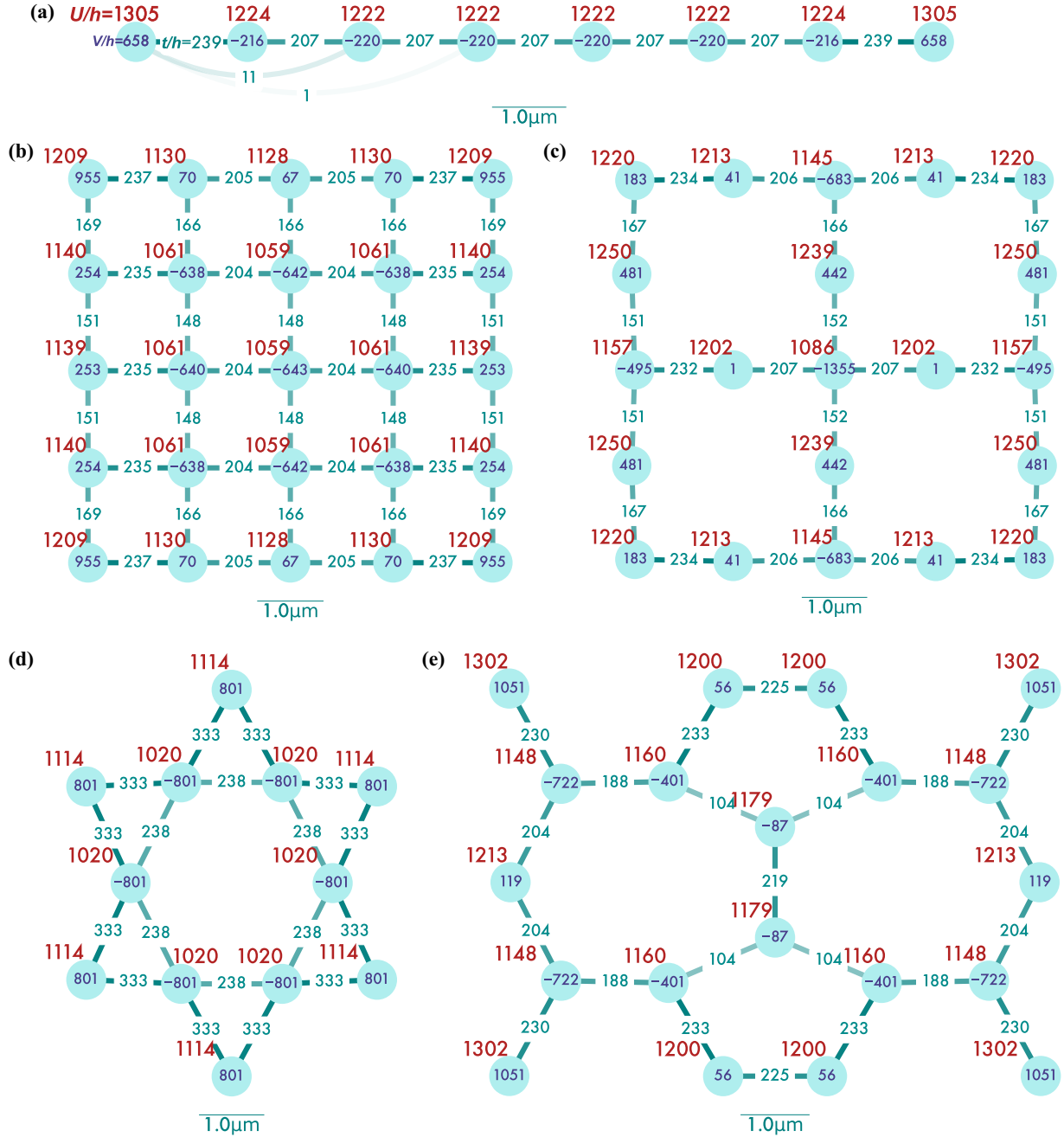
FIG. 3. Hubbard parameters calculated for (a) an eight-site chain, (b) a 5×5 rectangle, (c) 2×2 Lieb plaquettes, (d) a star of David (kagome plaquette), and (e) a honeycomb lattice with a Stone-Wales defect. Each node of the graph shown is centered at the Wannier-function peak position. Numbers offset from the nodes are on-site interactions U, those inside circles are on-site potentials V, and those on bonds are tunnelings t, all in units of $h \times$ Hz. For each geometry, we shift the V_i so that their average is zero since only relative differences between V_i have physical meaning. The transparency of bonds reflects the tunneling strength. Further-neighbor tunnelings are shown in (a) but omitted elsewhere. Tweezer parameters are specified in the text.

In the following, we present the results of equalizing Hubbard parameters to uniform target values. We will present results from three protocols: The first two use only capabilities demonstrated in existing experiments (we adjust only the trap positions r_i and depths V_{0i}), while the third also allows the tweezer waists w_i to be tuned, and we suggest a method to accomplish this.

B. Equalization with previously demonstrated tweezer techniques

We first try to equalize Hubbard parameters based on how previous experiments [21,23] were performed: We adjust the trap positions r_i and depths V_{0i}. The results are shown in Fig. 5. In all the diagrams, especially Fig. 5(b), we can see how equalizing Hubbard parameters requires distorting the
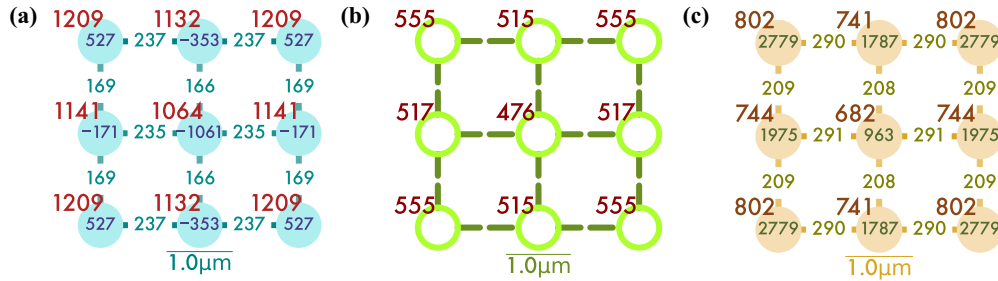
FIG. 4. Two-band Hubbard parameters for (a) the first band, (b) interband interactions between the first band and the z excited band, and (c) the z excited band. The z direction is out of the plane, and the z excited band is the lowest-energy excited band for the parameters considered, as described in the text.

experimental trap parameters. In Fig. 5 (and following figures), the positions of the nodes are located at the peaks of the Wannier functions; the transparency of nodes shows the relative depths of trap V_{0i} compared to the trap with maximum depth.

From Fig. 5, we can see that although the total variation of V over the lattice is suppressed to less than $\sim h \times 5$ Hz, the differences for interaction U and tunneling t are only modestly improved compared to the uniform trap configurations, such as results in Figs. 3 and 4. (The squared variation is reduced by a few percent, while the maximum difference can even increase slightly.) This is particularly severe if we think of the most sensitive energy scale $\tilde{t}$ in the Hubbard model, as the maximal fluctuation of U is as large as $\tilde{t}$. The variation is the most significant when comparing boundary and bulk sites. And comparing various lattices, it is more severe in lattices with more neighbors.

It is natural that not all parameters can be equalized since the number of Hubbard parameters is larger than the number of tunable trap parameters. For example, a large anisotropic square lattice has roughly four Hubbard parameters per trap (t_x, t_y, U, and V) but only three parameters to tune per trap (x and y locations and trap depth V_{0i}). Trade-offs can be made in the accuracies of $t_{x,y}$, V, and U by reweighting the terms in the cost function (16), but at best one can equalize two parameters fairly accurately.

In order to fully equalize all the Hubbard parameters, more degrees of freedom must be introduced. Here we present two

proposals to achieve that goal: the first uses extra "ghost traps" on the edges and uses only tuning of trap parameters already demonstrated in experiment (positions and depths), and the second uses "trap-dependent waists." The ghost-traps proposal is the more feasible approach with current experimental capabilities but still must be handled with care (keeping ghost traps sufficiently distinct to avoid beating and requiring slightly more laser power to generate ghost-trap layers). The trap-dependent-waist proposal is more speculative and has challenges in obtaining sufficient flexibility in tuning the waists with AOMs or the stability of SLMs but, nevertheless, conceivably could be developed into a useful tool.

C. Proposal 1 for improved equalization: Ghost sites

The first proposal to equalize Hubbard parameters is to add ghost sites, as shown in Fig. 1(d). Inspired by the observation that the Hubbard parameter nonuniformity is mostly near system edges, an experiment can simply be restricted to measurements on sites away from the edges and can obtain good uniformity. If, additionally, one optimizes for uniformity only on sites not along the edge by including only nonedge sites in the cost function, the parameters can be made uniform (we obtain a 2×10^{-4} relative variation between parameters in the example, with error that is set by the optimization algorithm tolerance, rather than a fundamental limitation of the protocol). This is illustrated for the chain and square lattices in Figs. 6(a) and 6(c). This protocol is
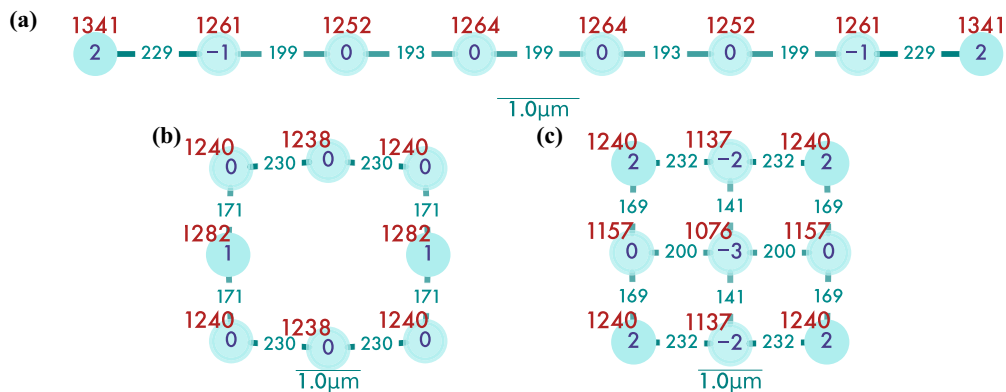

FIG. 5. Hubbard parameters for trap parameters that give the closest-to-equalized Hubbard parameters [according to Eq. (16)] achievable by varying trap position and depth for (a) an eight-site chain, (b) one Lieb plaquette, and (c) a 3×3 rectangular lattice. Number labels are as in Fig. 3.
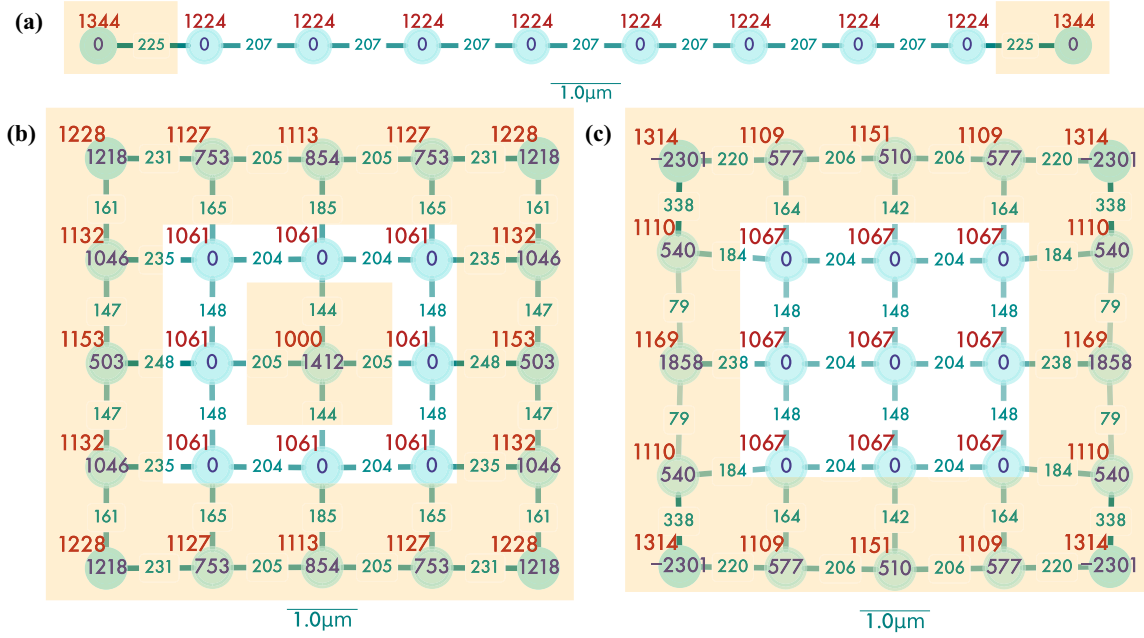
FIG. 6. Hubbard parameters equalized as in Fig. 5, augmented with "ghost sites" on the boundaries for (a) an eight-site chain, (b) one Lieb plaquette, and (c) a 3×3 rectangular lattice. Number labels are as in Fig. 3.

suitable when one is studying lattices of simple patterns, such as 1D chain or 2D square lattices. Then physical quantities such as the particle number in the edge sites (ghost traps) are not included in measurements of observables for the purposes of quantum simulation. In this way, the edges can be seen as a special boundary condition to the rest of the tweezer array.

A slightly more difficult case in which to employ ghost traps is a lattice such as the Lieb plaquette, as several boundaries occur not as the edges of a large array, but within each unit cell. Another example is when one wants to study a finite-size Hubbard system with sharp edges. In this case, ghost traps can still be used, but one must ensure that particles do not occupy the ghost traps. This can be done by ensuring the on-site potential on the ghost traps is large enough to prevent occupation, which is done by giving the equalization algorithm a $5\% \times V_0 \approx h \times 2500\,\text{Hz}$ smaller initial value for V_0 on the center ghost trap, which is about one order of magnitude larger than tunnelings. Figure 6(b) shows that this approach again works well for the Lieb plaquette by applying the special initial guess for the central ghost trap "inside" the plaquette. This relative error is better than 2×10^{-4} and is controlled by the optimization convergence criterion, with a central ghost trap having $V_i = h \times 1400\,\text{Hz}$.

D. Proposal 2 for improved equalization: Tunable tweezer trap waists

Adding ghost traps is effective but requires sacrificing many traps (and associated laser power and imaging region) to traps that are not being measured. Ghost traps are lattice geometry specific, and they might not work well for irregular lattice geometries, such as a lattice with a Stone-Wales defect, as shown in Fig. 3(e). Additionally, although we do not explore it here, it would not provide any significant ability to

engineer higher bands' Hubbard parameters. In this section, we introduce a second method that offers more tuning parameters and does not require additional traps.

This second proposal is to adjust each tweezer trap waist w_i individually, as shown in Fig. 1(a), which increases the number of trap parameters and gives a natural way to tune U_i, V_i, and t_{ij} more independently. Although site-dependent waists have not been demonstrated in experiment, one idea to change the width of each trap individually is to program it using the same stroboscopic averaging that is used to create the tweezers in the first place [23]. There may be limited control of the exact shape created due to imaging resolution and rate of strobing, but some control on trap width should be possible.

The Hubbard parameters after optimizing using these additional degrees of freedom are shown in Fig. 7. We vary only waists $w_{i,x}$ in the x direction in the 1D chain in Fig. 7(a), while for the more complicated 2D systems shown in Figs. 7(b) and 7(c), we allow for both x- and y-direction waists $w_{i,x}$ and $w_{i,y}$ to vary.

IV. CONCLUSION

We have calculated the effective Hubbard model parameters for programmable fermionic optical tweezer arrays, a novel platform for quantum simulations and computation. We used a combination of a DVR method to obtain single-particle eigenstates, truncating these to the target energy band, and optimizing over the manifold of unitary transformations for that energy subspace to obtain the MLWF. We found that this method allowed us to efficiently calculate Hubbard parameters. We also presented results for several geometries: finite 1D chains, 2D square lattices, Lieb lattices, and hexagonal lattices with Stone-Wales defects. Multiband calculations were demonstrated for a two-band square lattice. We note
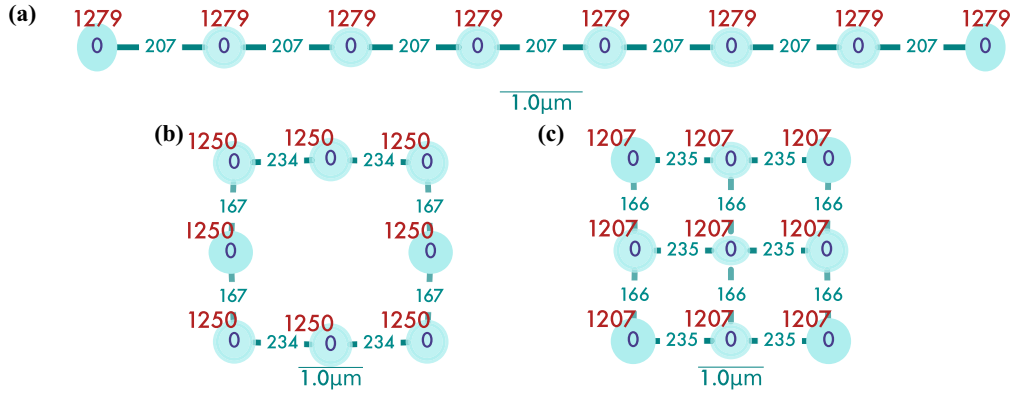
FIG. 7. Hubbard parameters equalized as in Fig. 5 and also allowing waists to vary: (a) an eight-site chain allowing the x-direction waist to vary and (b) a Lieb plaquette and (c) a 3×3 rectangular lattice allowing trap waists to vary in the x and y directions. The shape of each node shows the ratio between distorted trap waists in the x and y directions. Number labels are as in Fig. 3.

that the method is immediately applicable to other systems, including bosonic atoms and long-range interacting systems, such as lanthanide atoms [49–51], polar molecules [37,38,52–54], and Rydberg-dressed atoms [40,41,55]. In addition, our methods are equally effective for recently developed hybrid lattice-tweezer architectures, such as optical lattices with programmable site-block tweezer beams [56] and optical quasicrystals realized by a set of incommensurate-wavelength laser beams [35,57].

One feature revealed by our results is that even though a tweezer geometry may be uniform (equal spacings and depths for all traps), the resulting Hubbard parameters may be nonuniform. This effect is most pronounced near the edges of the trap arrays.

Since researchers often want to study spatially uniform Hubbard models, we introduced and demonstrated protocols to design trap-array parameters to achieve this. We expect that optimization with an appropriately chosen cost function should also allow us to determine trap parameters that lead to desired nonuniform Hubbard models. The enhancement of the programmability of tweezer arrays could further contribute to the realization of the proposed fermionic gate design and control [58,59].

Although published experiments with tunnel-coupled tweezers [17,18,21,23] have worked with modest-sized systems having at most ∼50 traps, experiments with hundreds or perhaps thousands of sites and atoms seem possible by extending current techniques. Experiments with tweezer arrays of Rydberg atoms now routinely work with over 100 atoms. For example, recent experiments have reached 225 sites to achieve a perfect filling of one atom per trap [60] over 33% of the time in a room-temperature apparatus. Cryogenic experiments can offer even larger arrays [61]. And there are clear routes to increasing this number. There are no fundamental obstacles to applying the same techniques to tunnel-coupled tweezers. Our code readily handles such cases, scaling well with the number of traps N_{trap}. The time and memory required for DVR calculations scale no worse than N_{trap}^2. The time and memory costs to find the unitary basis transformation are negligible and scale no worse than DVR. In practice, we are able to calculate the Hubbard parameters of systems with 100 traps in about an hour on a laptop.

Our source code is publicly available on GitHub [62].

APPENDIX A: DVR CONVERGENCE

In the main text, we used the DVR grid-point spacing $\Delta x = (0.15, 0.15, 0.36)w_x$ and set the box size by setting the distance from the outermost trap centers to the system boundaries to $L_0 = (3, 3, 7.2)w_x$. This was shown to be highly converged for a single trap in Ref. [23]. We additionally checked the convergence in an eight-site chain Hubbard parameter calculation by comparing values of t, U, and V among different grid-point spacings Δx and ranges L_0. In addition, we also checked the U numerical integration convergence by varying the number of points in the integration grid. All of the above results are summarized in Fig. 8, indicating good convergence for the results presented in the main text. Based on these results, we expect worst-case errors from all sources across all results in the text to be 10^{-8} or smaller. In the remainder of this Appendix, we will describe how the convergence of the algorithm was assessed.
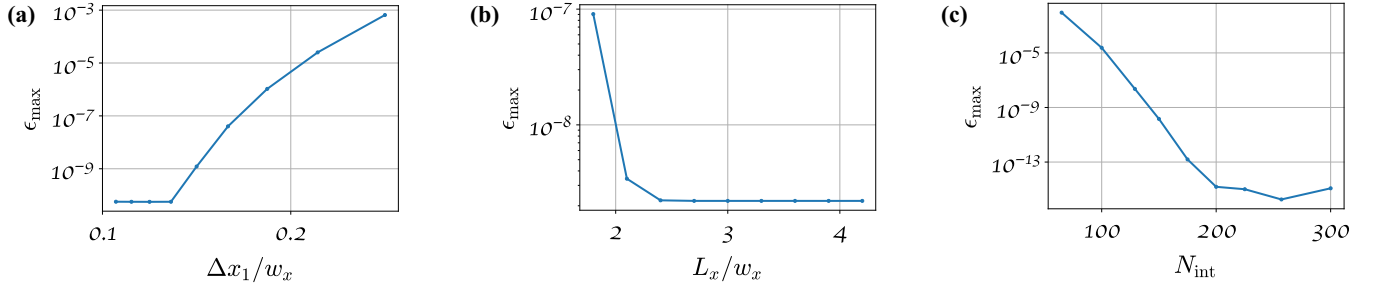
FIG. 8. The maximal error of eight-site-chain Hubbard parameters vs DVR grid spacing $\Delta x = (1, 1, 2.4) \times \Delta x_1$, grid range $L_0 = (1, 1, 2.4) \times L_x$, and numerical integration grid-point number N_{int}. The definition of each quantity is explained in Appendix A.

We characterize the error of a given Hubbard parameter by extrapolating the convergence parameter (e.g., grid spacing Δx or spatial buffer size L_0) to its fully converged value (e.g., $\Delta x \to 0$ or $L_0 \to \infty$) and then calculating its maximum relative error over the whole geometry ϵ_{max}, defining the error as the relative difference between the grid being assessed and the extrapolated grid:

$$\epsilon_{\text{max}} = \max_i \frac{\left| q_i^{(\text{choice})} - q_i^* \right|}{|q_i^*|}. \tag{A1}$$

Here q_i can be any Hubbard parameter t_{ij}, V_i, or U_i, and the site (bond) index i is over the entire lattice. $q_i^{(\text{choice})}$ means q_i is calculated for some convergence parameters, and q_i^* is the q_i extrapolated at the infinitely fine grid.

The extrapolation is performed by fitting the three most accurate grid choices for the quantity q_i using the exponential function:

$$q_i^{(\text{choice})}(N) = ae^{-bN} + c, \tag{A2}$$

where N is the grid fineness parameter. It can be $N_{\Delta x}$, N_L, or N_{int}, whose definitions are given below. The extrapolation is performed to $N \to \infty$, so that $q_i^* = c$ for each fit.

Figure 8(a) shows the convergence with the DVR grid spacing Δx. We consider results for grid spacings $\Delta x = L_0/N_{\Delta x}$ with $N_{\Delta x} = 12, 14, \ldots, 28$, and we fix $L_0 = (3, 3, 7.2)w_x$. These spacings range from $\Delta x^* = (0.107, 0.107, 0.0257)w_x$ to $(0.25, 0.25, 0.6)w_x$. The grid spacing we use in the main text corresponds to $N_{\Delta x} = 20$. These results suggest the grid-spacing convergence error is as small as 10^{-9} for calculations in the main text.

Figure 8(b) shows the convergence with the total size of the DVR box, measured by L_0. We vary L_0 over $L_0 = (0.15, 0.15, 0.36)w_x \times N_L$, where $N_L = 12, 14, \ldots, 28$, and we fix $\Delta x = (0.15, 0.15, 0.36)w_x$, with the best convergence at $L_0^* = (4.2, 4.2, 10.08)w_x$. The box size we use in the main text is $N_L = 20$. These results show that the box-size convergence error is on the order of 10^{-9}. We see this error saturates to the error from Δx.

Finally, Fig. 8(c) shows the convergence of U with the numerical integration grid density. We choose the numerical integration region to extend to 1.2 times the DVR box and the integration grid spacing to be set by the number of grid points in each dimension N_{int}. In the main text, we use $N_{\text{iint}} = 257$. The results show that the numerical integration converges to the order of machine precision.

For the higher-band case, we expect error convergence to be similarly exponential, but with a slightly larger prefactor, according to calculations in [31].

In summary, all of our Hubbard parameter systematic numerical errors are under control to an error less than 10^{-8}. And our parameter choices are close to saturation.

APPENDIX B: PROOF OF ALL-REAL MLWF TRANSFORMATION-MATRIX ENTRIES

In this Appendix, we prove that in our case, all entries in the MLWF unitary transformation matrix $D_{ia}^{(\mu)}$ can be chosen to be real. This means it can be reduced to the special orthogonal matrix. This stems from the fact that the tweezer trapping continuum Hamiltonian is real. Without loss of generality, we suppress the band index μ for the derivation.

Our starting point is the cost function (12) to minimize in the main text to find MLWFs:

$$\tilde{\Omega} = \sum_\xi \sum_{i \neq j} |\langle W_i | r_\xi | W_j \rangle|^2$$

$$= \sum_\xi \sum_{i \neq j} \left| \sum_{ab} (D_{ia})^* D_{jb} R_{\xi, ab} \right|^2, \tag{B1}$$

where $R_{\xi, ab} \equiv \langle \phi_a | r_\xi | \phi_b \rangle$ is shorthand for matrix elements of position operators in the eigenbasis $\{|\phi_a\rangle\}$.

Since the continuum Hamiltonian is real, it can be proven that the eigenstates can all be real. Think of the complex conjugate of the eigenequation of ϕ_a with eigenenergy ϵ_a:

$$H^* \phi_a^* = \epsilon_a^* \phi_a^* \to H \phi_a^* = \epsilon_a \phi_a^*. \tag{B2}$$

Because both H and ϵ_a are real, ϕ_a^* is the degenerate eigenstate of the same eigenenergy. Proper linear combinations of ϕ_a and ϕ_a^* lead to two real solutions. Therefore, we claim that $R_{\xi, ab}$ matrices are Hermitian and real.

As mentioned in the main text, this function is nonnegative, and the zero value can be taken if $R_\xi = X, Y, Z$ can be simultaneously diagonalized. In a 1D lattice, only the $R_\xi = X$ matrix would be nonzero due to reflection symmetry, and the minimum of $\tilde{\Omega}$ is found at the D_{ia} diagonalizing X_{ab}. This D_{ia} is orthogonal (has only real entries) because eigenstates of the real Hermitian matrices $R_{\xi, ab}$ can be chosen to be real, with the reason illustrated above.

For higher dimensions the D_{ia} that minimize $\tilde{\Omega}$ are no longer the eigensolutions of X_{ab}, as the matrices R_ξ are basis dependent and in general don't commute. The optimization needs to be done numerically.

Nevertheless, the matrix D_{ia} can be simplified to be real entries by the following proof.

Since we cannot find a single real (orthogonal) matrix to diagonalize three R_ξ, we find three orthogonal matrices O^ξ to diagonalize the real Hermitian matrices $R_{\xi,ab}$, respectively:

$$R_{\xi,ab} = \sum_{mn} r_{\xi,m} \delta_{mn} O^\xi_{am} O^\xi_{bn}, \tag{B3}$$

where $r_{\xi,m}$ is the mth eigenvalue of matrix R_ξ.

Then we decompose the unitary matrix into two matrices $D_{ia} = \sum_b O^\xi_{ab} Z^\xi_{bi}$, where we absorb all complex phases into the ξ-dependent matrix Z^ξ. It is clear that Z^ξ is unitary as well.

For each ξ we can expand the terms in cost function (B1) and simplify the equation by substituting O^ξ:

$$\sum_{i \neq j} \left| \sum_{ab} (D_{ia})^* D_{jb} R_{\xi,ab} \right|^2$$

$$= \sum_{i \neq j} \left| \sum_{ab} (D_{ia})^* D_{jb} \sum_{mn} r_{\xi,m} \delta_{mn} O^\xi_{am} O^\xi_{bn} \right|^2$$

$$= \sum_{i \neq j} \left| \sum_{ab} (D_{ia})^* D_{jb} \sum_m r_{\xi,m} O^\xi_{am} O^\xi_{bm} \right|^2$$

$$= \sum_{i \neq j} \sum_m \left| (Z^\xi_{mi})^* Z^\xi_{mj} r_{\xi,m} \right|^2. \tag{B4}$$

The above occurs because of the orthogonality of O^ξ. We then expand the complex modulus:

$$\sum_{i \neq j} \sum_m \left| (Z^\xi_{mi})^* Z^\xi_{mj} r_{\xi,m} \right|^2$$

$$= \sum_{i \neq j} \sum_m (Z^\xi_{mi})^* Z^\xi_{mj} r_{\xi,m} \sum_n (Z^\xi_{nj})^* Z^x_{ni} r_{\xi,n}$$

$$= \sum_{mn} r_{\xi,m} r_{\xi,n} \sum_{i \neq j} (Z^\xi_{mi} Z^\xi_{nj})^* Z^\xi_{ni} Z^\xi_{mj}. \tag{B5}$$

Now we focus on the only complex part:

$$\sum_{i \neq j} (Z^\xi_{mi} Z^\xi_{nj})^* Z^\xi_{ni} Z^\xi_{mj}$$

$$= \left(\sum_{ij} - \sum_{i=j} \right) (Z^\xi_{mi} Z^\xi_{nj})^* Z^\xi_{ni} Z^\xi_{mj}$$

$$= \sum_i (Z^\xi_{mi})^* Z^\xi_{ni} \sum_j (Z^\xi_{nj})^* Z^\xi_{mj} - \sum_i (Z^\xi_{mi} Z^\xi_{ni})^* Z^\xi_{mi} Z^\xi_{ni}$$

$$= \delta_{mn} - \sum_i |Z^\xi_{mi}|^2 |Z^\xi_{ni}|^2. \tag{B6}$$

The last Kronecker delta is from the fact that Z^ξ is unitary, and $\delta^2_{mn} = \delta_{mn}$.

We can see that every factor in the expression of $\tilde{\Omega}$ is independent of the phase of any unitary matrix entry Z^ξ_{mi}. So it suffices to assume all entries of D_{ia} are real.

[1] M. Imada, A. Fujimori, and Y. Tokura, Metal-insulator transitions, Rev. Mod. Phys. **70**, 1039 (1998).

[2] *The Hubbard Model: A Reprint Volume*, edited by A. Montorsi (World Scientific, Singapore, 1992).

[3] H. Tasaki, The Hubbard model - an introduction and selected rigorous results, J. Phys.: Condens. Matter **10**, 4353 (1998).

[4] D. P. Arovas, E. Berg, S. A. Kivelson, and S. Raghu, The Hubbard model, Annu. Rev. Condens. Matter Phys. **13**, 239 (2022).

[5] M. Qin, T. Schäfer, S. Andergassen, P. Corboz, and E. Gull, The Hubbard model: A computational perspective, Annu. Rev. Condens. Matter Phys. **13**, 275 (2022).

[6] The Hubbard model at half a century, Nat. Phys. **9**, 523 (2013).

[7] T. Esslinger, Fermi-Hubbard physics with atoms in an optical lattice, Annu. Rev. Condens. Matter Phys. **1**, 129 (2010).

[8] I. M. Georgescu, S. Ashhab, and F. Nori, Quantum simulation, Rev. Mod. Phys. **86**, 153 (2014).

[9] L. Tarruell and L. Sanchez-Palencia, Quantum simulation of the Hubbard model with ultracold fermions in optical lattices, C. R. Phys. **19**, 365 (2018).

[10] I. Bloch, J. Dalibard, and S. Nascimbène, Quantum simulations with ultracold quantum gases, Nat. Phys. **8**, 267 (2012).

[11] C. Gross and I. Bloch, Quantum simulations with ultracold atoms in optical lattices, Science **357**, 995 (2017).

[12] C. Gross and W. S. Bakr, Quantum gas microscopy for single atom and spin detection, Nat. Phys. **17**, 1316 (2021).

[13] A. Bohrdt, L. Homeier, C. Reinmoser, E. Demler, and F. Grusdt, Exploration of doped quantum magnets with ultracold atoms, Ann. Phys. (NY) **435**, 168651 (2021).

[14] E. Altman *et al.*, Quantum simulators: Architectures and opportunities, PRX Quantum **2**, 017003 (2021).

[15] A. Mazurenko, C. S. Chiu, G. Ji, M. F. Parsons, M. Kanász-Nagy, R. Schmidt, F. Grusdt, E. Demler, D. Greif, and M. Greiner, A cold-atom Fermi–Hubbard antiferromagnet, Nature (London) **545**, 462 (2017).

[16] S. Taie, E. Ibarra-García-Padilla, N. Nishizawa, Y. Takasu, Y. Kuno, H.-T. Wei, R. T. Scalettar, K. R. A. Hazzard, and Y. Takahashi, Observation of antiferromagnetic correlations in an ultracold SU(N) Hubbard model, Nat. Phys. **18**, 1356 (2022).

[17] A. M. Kaufman, B. J. Lester, C. M. Reynolds, M. L. Wall, M. Foss-Feig, K. R. A. Hazzard, A. M. Rey, and C. A. Regal, Two-particle quantum interference in tunnel-coupled optical tweezers, Science **345**, 306 (2014).

[18] S. Murmann, A. Bergschneider, V. M. Klinkhamer, G. Zürn, T. Lompe, and S. Jochim, Two fermions in a double well:

Exploring a fundamental building block of the Hubbard model, Phys. Rev. Lett. **114**, 080402 (2015).

[19] A. Bergschneider, V. M. Klinkhamer, J. H. Becher, R. Klemt, L. Palm, G. Zürn, S. Jochim, and P. M. Preiss, Experimental characterization of two-particle entanglement through position and momentum correlations, Nat. Phys. **15**, 640 (2019).

[20] J. H. Becher, E. Sindici, R. Klemt, S. Jochim, A. J. Daley, and P. M. Preiss, Measurement of identical particle entanglement and the influence of antisymmetrization, Phys. Rev. Lett. **125**, 180402 (2020).

[21] B. M. Spar, E. Guardado-Sanchez, S. Chi, Z. Z. Yan, and W. S. Bakr, Realization of a Fermi-Hubbard optical tweezer array, Phys. Rev. Lett. **128**, 223202 (2022).

[22] Y. Florshaim, E. Zohar, D. Zeev Koplovich, I. Meltzer, R. Weill, J. Nemirovsky, A. Stern, and Y. Sagi, Spatial adiabatic passage of ultracold atoms in optical tweezers, arXiv:2305.16228.

[23] Z. Z. Yan, B. M. Spar, M. L. Prichard, S. Chi, H.-T. Wei, E. Ibarra-García-Padilla, K. R. A. Hazzard, and W. S. Bakr, Two-dimensional programmable tweezer arrays of fermions, Phys. Rev. Lett. **129**, 123201 (2022).

[24] J. P. Hague, L. Petit, and C. MacCormick, Analytic expressions for Hubbard models with arbitrary structures in programmable optical lattices, Phys. Rev. A **104**, 053321 (2021).

[25] J. Light and T. Carrington, Discrete-variable representations and their utilization, Adv. Chem. Phys. **114**, 263 (2000).

[26] N. Nygaard, G. M. Bruun, C. W. Clark, and D. L. Feder, Microscopic structure of a vortex line in a dilute superfluid Fermi gas, Phys. Rev. Lett. **90**, 210402 (2003).

[27] N. Nygaard, G. M. Bruun, B. I. Schneider, C. W. Clark, and D. L. Feder, Vortex line in a neutral finite-temperature superfluid Fermi gas, Phys. Rev. A **69**, 053622 (2004).

[28] R. G. Littlejohn, M. Cargo, T. Carrington Jr., K. A. Mitchell, and B. Poirier, A general framework for discrete variable representation basis sets, J. Chem. Phys. **116**, 8691 (2002).

[29] B. Fornberg, *A Practical Guide to Pseudospectral Methods*, Cambridge Monographs on Applied and Computational Mathematics (Cambridge University Press, Cambridge, UK, 1996).

[30] D. T. Colbert and W. H. Miller, A novel discrete variable representation for quantum mechanical reactive scattering via the S-matrix Kohn method, J. Chem. Phys. **96**, 1982 (1992).

[31] M. L. Wall, K. R. A. Hazzard, and A. M. Rey, Effective many-body parameters for atoms in nonseparable Gaussian optical potentials, Phys. Rev. A **92**, 013610 (2015).

[32] N. Marzari, A. A. Mostofi, J. R. Yates, I. Souza, and D. Vanderbilt, Maximally localized Wannier functions: Theory and applications, Rev. Mod. Phys. **84**, 1419 (2012).

[33] M. Modugno and G. Pettini, Maximally localized Wannier functions for ultracold atoms in one-dimensional double-well periodic potentials, New J. Phys. **14**, 055004 (2012).

[34] J. Ibañez-Azpiroz, A. Eiguren, A. Bergara, G. Pettini, and M. Modugno, Tight-binding models for ultracold atoms in honeycomb optical lattices, Phys. Rev. A **87**, 011602(R) (2013).

[35] E. Gottlob and U. Schneider, Hubbard models for quasicrystalline potentials, Phys. Rev. B **107**, 144202 (2023).

[36] X. Qiu, J. Zou, X. Qi, and X. Li, Precise programmable quantum simulations with optical lattices, npj Quantum Inf. **6**, 87 (2020).

[37] A. V. Gorshkov, S. R. Manmana, G. Chen, J. Ye, E. Demler, M. D. Lukin, and A. M. Rey, Tunable superfluidity and quantum magnetism with ultracold polar molecules, Phys. Rev. Lett. **107**, 115301 (2011).

[38] B. Yan, S. A. Moses, B. Gadway, J. P. Covey, K. R. A. Hazzard, A. M. Rey, D. S. Jin, and J. Ye, Observation of dipolar spin-exchange interactions with lattice-confined polar molecules, Nature (London) **501**, 521 (2013).

[39] J. W. Park, S. A. Will, and M. W. Zwierlein, Ultracold dipolar gas of fermionic ^{23}Na^{40}K molecules in their absolute ground state, Phys. Rev. Lett. **114**, 205302 (2015).

[40] N. Defenu, T. Donner, T. Macrì, G. Pagano, S. Ruffo, and A. Trombettoni, Long-range interacting quantum systems, Rev. Mod. Phys. **95**, 035002 (2023).

[41] J. E. Johnson and S. L. Rolston, Interactions between Rydberg-dressed atoms, Phys. Rev. A **82**, 033412 (2010).

[42] X. Li and S. Das Sarma, Exotic topological density waves in cold atomic Rydberg-dressed fermions, Nat. Commun. **6**, 7137 (2015).

[43] J. Townsend, N. Koep, and S. Weichwald, Pymanopt: A python toolbox for optimization on manifolds using automatic differentiation, J. Mach. Learn. Res. **17**, 1 (2016).

[44] Utilizing anisotropic lattice constants allows experiments to avoid low-frequency beatings at diagonal sites [23].

[45] S. Taie, H. Ozawa, T. Ichinose, T. Nishio, S. Nakajima, and Y. Takahashi, Coherent driving and freezing of bosonic matter wave in an optical Lieb lattice, Sci. Adv. **1**, e1500854 (2015).

[46] G.-B. Jo, J. Guzman, C. K. Thomas, P. Hosur, A. Vishwanath, and D. M. Stamper-Kurn, Ultracold atoms in a tunable optical kagome lattice, Phys. Rev. Lett. **108**, 045305 (2012).

[47] M. Melchner Von Dydiowa, Quantum simulation with an optical kagome lattice, Ph.D. thesis, University of Cambridge, 2022.

[48] M. T. Lusk and L. D. Carr, Nanoengineering defect structures on graphene, Phys. Rev. Lett. **100**, 175503 (2008).

[49] M. A. Norcia and F. Ferlaino, Developments in atomic control using ultracold magnetic lanthanides, Nat. Phys. **17**, 1349 (2021).

[50] H. Li, J.-F. Wyart, O. Dulieu, and M. Lepers, Anisotropic optical trapping as a manifestation of the complex electronic structure of ultracold lanthanide atoms: The example of holmium, Phys. Rev. A **95**, 062508 (2017).

[51] M. Li, E. Tiesinga, and S. Kotochigova, Orbital quantum magnetism in spin dynamics of strongly interacting magnetic lanthanide atoms, Phys. Rev. A **97**, 053627 (2018).

[52] A. M. Kaufman and K.-K. Ni, Quantum science with optical tweezer arrays of ultracold atoms and molecules, Nat. Phys. **17**, 1324 (2021).

[53] K. R. A. Hazzard, S. R. Manmana, M. Foss-Feig, and A. M. Rey, Far-from-equilibrium quantum magnetism with ultracold polar molecules, Phys. Rev. Lett. **110**, 075301 (2013).

[54] G. Natale, R. M. W. van Bijnen, A. Patscheider, D. Petter, M. J. Mark, L. Chomaz, and F. Ferlaino, Excitation spectrum of a trapped dipolar supersolid and its experimental evidence, Phys. Rev. Lett. **123**, 050402 (2019).

[55] Y. Zhou, Y. Li, R. Nath, and W. Li, Quench dynamics of Rydberg-dressed bosons on two-dimensional square lattices, Phys. Rev. A **101**, 013427 (2020).

[56] D. Wei, D. Adler, K. Srakaew, S. Agrawal, P. Weckesser, I. Bloch, and J. Zeiher, Observation of brane parity order in programmable optical lattices, Phys. Rev. X **13**, 021042 (2023).

[57] K. Viebahn, M. Sbroscia, E. Carter, J.-C. Yu, and U. Schneider, Matter-wave diffraction from a quasicrystalline optical lattice, Phys. Rev. Lett. **122**, 110404 (2019).

[58] D. González-Cuadra, D. Bluvstein, M. Kalinowski, R. Kaubruegger, N. Maskara, P. Naldesi, T. V. Zache, A. M. Kaufman, M. D. Lukin, H. Pichler, B. Vermersch, J. Ye, and P. Zoller, Fermionic quantum processing with programmable neutral atom arrays, Proc. Natl. Acad. Sci. USA **120**, e2304294120 (2023).

[59] Q. Li, C. Mukhopadhyay, and A. Bayat, Fermionic simulators for enhanced scalability of variational quantum simulation, Phys. Rev. Res. **5**, 043175 (2023).

[60] W. Tian, W. J. Wee, A. Qu, B. J. M. Lim, P. R. Datla, V. P. W. Koh, and H. Loh, Parallel assembly of arbitrary defect-free atom arrays with a multitweezer algorithm, Phys. Rev. Appl. **19**, 034048 (2023).

[61] K.-N. Schymik, B. Ximenez, E. Bloch, D. Dreon, A. Signoles, F. Nogrette, D. Barredo, A. Browaeys, and T. Lahaye, *In situ* equalization of single-atom loading in large-scale optical tweezer arrays, Phys. Rev. A **106**, 022611 (2022).

[62] H.-T. Wei, HUBBARDTWEEZER version 0.5.0: Calculate Hubbard parameters in optical tweezer array systems,2023, doi:10.5281/zenodo.8364496.